Soft Matter

PAPER

View Article Online
View Journal | View Issue

Cite this: *Soft Matter*, 2016, 12, 8927

Perpetual superhydrophobicity

Alberto Giacomello,*[ab] Lothar Schimmele,[b] Siegfried Dietrich[bc] and Mykola Tasinkevych*[bc]

Received 27th July 2016,
Accepted 5th October 2016

DOI: 10.1039/c6sm01727d

www.rsc.org/softmatter

A liquid droplet placed on a geometrically textured surface may take on a "suspended" state, in which the liquid wets only the top of the surface structure, while the remaining geometrical features are occupied by vapor. This superhydrophobic Cassie–Baxter state is characterized by its composite interface which is intrinsically fragile and, if subjected to certain external perturbations, may collapse into the fully wet, so-called Wenzel state. Restoring the superhydrophobic Cassie–Baxter state requires a supply of free energy to the system in order to again nucleate the vapor. Here, we use microscopic classical density functional theory in order to study the Cassie–Baxter to Wenzel and the reverse transition in widely spaced, parallel arrays of rectangular nanogrooves patterned on a hydrophobic flat surface. We demonstrate that if the width of the grooves falls below a threshold value of *ca.* 7 nm, which depends on the surface chemistry, the Wenzel state becomes thermodynamically unstable even at very large positive pressures, thus realizing a "*perpetual*" superhydrophobic Cassie–Baxter state by passive means. Building upon this finding, we demonstrate that hierarchical structures can achieve perpetual superhydrophobicity even for micron-sized geometrical textures.

1 Introduction

Superhydrophobicity refers to an important class of surface properties which include self cleaning,[1] liquid repellency,[2] anti-(bio)fouling, drag reduction,[3] *etc.* Superhydrophobicity is achieved by combining surface roughness and wetting properties† such that the geometrical features of the surface are filled by vapor.[5] This corresponds to the so-called Cassie–Baxter state for which the liquid is in contact only with the topmost portions of the surface. This "suspended" state is fragile because the composite (solid/liquid plus liquid/vapor) interface may collapse into the fully wet Wenzel state in which the superhydrophobic properties are lost. The technological applications of superhydrophobicity are therefore severely limited by its fragility: depending on the environmental conditions and on the wetting history, a surface may or may not exhibit superhydrophobic properties. Here, we show that a class of nano-sized roughnesses is capable of destabilizing the Wenzel state thermodynamically, thus realizing virtually perpetual and robust superhydrophobicity.

On rough hydrophobic surfaces the Cassie–Baxter state can be either stable or metastable depending on the thermodynamic conditions (*e.g.*, pressure and temperature).[6] The transition from the (meta)stable Cassie–Baxter state to the Wenzel state requires to overcome free energy barriers much larger than the thermal energy k_BT, even for surface asperities of a few nanometers in size.[7,8] These metastabilities generate strong hysteresis in the wetting and dewetting processes on such surfaces.[9] On the other hand, the large free energy barriers also imply that once the system has occupied the Wenzel state, superhydrophobicity cannot be restored without supplying free energy to the system.

In order to restore superhydrophobicity from the Wenzel state the most effective strategy to date seems to be the application of an electric field to the system.[10–12] Other methods include a magnetically driven Wenzel to Cassie–Baxter transition[13] and heating of the surface until boiling restores the vapor pockets.[14] All these active methods require special preparations of the surface and/or of the liquid as well as a free energy source; in addition, they cannot be easily applied to large surfaces.

Passive methods for restoring superhydrophobicity are in principle more economical and general than active ones. One strategy for trying to passively "stabilize" the Cassie–Baxter state is to shrink the size of surface decorations down to the nanoscale.[15] For instance, by using carefully designed hydrophobic

[a] *Sapienza Università di Roma, Dipartimento di Ingegneria Meccanica e Aerospaziale, 00184 Rome, Italy. E-mail: alberto.giacomello@uniroma1.it; Tel: +39 06 44585200*
[b] *Max-Planck-Institut für Intelligente Systeme, 70569 Stuttgart, Germany. E-mail: miko@mf.mpg.de; Tel: +49 711 689-1949*
[c] *IV. Institut für Theoretische Physik, Universität Stuttgart, 70569 Stuttgart, Germany*

† This generally requires a Young's contact angle $\theta_Y > 90°$. However, special reentrant[2] and doubly reentrant[4] textures can achieve a "superomniphobic" behavior, *i.e.*, they also repel liquids with $\theta_Y < 90°$.

nano-textures of *ca.* 10 nm size it was possible to support pressures up to several tens of atmospheres before mechanical destabilization of the Cassie–Baxter state takes place at a certain critical pressure P_c.[9] Verho *et al.* realized hierarchical structures *via* a regular texture (on the scale of *ca.* 10 μm) which is decorated by superhydrophobic silicon filaments (on the scale of 100 nm, grown on the micro-topography).[16] With this two-level topography the transitions between nano- and micron-sized Cassie–Baxter states offer the opportunity that they can be reversibly switched by using either local suction (recovering the micron-sized Cassie–Baxter state from the nano-sized one) or a jet of water at low pressures (creating the nano-sized Cassie–Baxter state from the micron-sized one). Such passive approaches provide several advantages, but they do not eliminate the potential occurrence of the transition to the Wenzel state, which can always be realized by thermally activated events or pressure changes.

The aim of the present study is to introduce a completely passive method, which involves the thermodynamic destabilization of the Wenzel state over a wide range of pressures above the bulk liquid–vapor coexistence pressure. In this way, a virtually perpetual superhydrophobic Cassie–Baxter state is realized which is the only one allowed thermodynamically within that pressure range. As shown below, this can be achieved by properly choosing the surface chemistry and by scaling the size of the surface roughness, here modeled as an array of rectangular grooves, down to the nanometer range. The required size of the roughness actually depends on the contact angle of the surface; in principle the approach could work even with groove widths w of the order of 7 nm. For such surfaces, the Wenzel state can be eliminated for pressures as high as 5 atm.

The idea of eliminating the Wenzel state is based on the well-known fact that liquids have a spinodal, *i.e.*, thermodynamic conditions for which the liquid state is unstable and disappears *via* cavitation. For pure liquids far from the critical point, the spinodal is observed at strongly negative pressures P (*i.e.*, tensile stresses applied to liquid). For example, for bulk water at ambient temperature this is estimated to be around −150 MPa.[17,18] However, by strongly confining the liquid it is possible to shift this spinodal to positive pressures P. This is known, *e.g.*, for macroscopically extended hard[19] and lyophobic slit pores[20] (see also ref. 21–23). In ref. 20 the authors estimate that for confined water the liquid spinodal reaches, upon varying the pore width w, the bulk liquid–vapor coexistence line $P_0(T)$ at $w \approx 5$ nm. Recent studies have proposed a special texture composed of a 2D square lattice of rectangular nano-pillars with added nano-particles at the centers of the lattice cells.[24] Since in the fully wet Wenzel state the liquid penetrates into the surface geometric features, the following question arises: is it possible to destabilize thermodynamically the liquid confined within the surface features at positive values of the pressure by decreasing the spatial extent of the features? This would provide a means to achieve a perpetual superhydrophobic Cassie–Baxter state. The present systematic study provides a positive answer to the above question.

2 Model

Here we employ microscopic, classical density functional theory (DFT) with the aim of determining for various systems the spinodal pressure P_{sp} of the confined liquid and the critical pressure P_c of destabilization of the Cassie–Baxter state. In particular, we study lyophobic nano-grooves of different widths (Fig. 1) and lyophobic slit pores.

DFT is based on the minimization of the grand potential functional

$$\Omega[\rho] = F[\rho] + \int \mathrm{d}^3 r\, \rho(\boldsymbol{r})[V(\boldsymbol{r}) - \mu], \qquad (1)$$

where $F[\rho]$ is the intrinsic Helmholtz free energy functional encompassing the fluid–fluid interactions, $\rho(\boldsymbol{r})$ is the fluid number density at position $\boldsymbol{r}$, $V(\boldsymbol{r})$ is the substrate potential, and μ is the chemical potential. The equilibrium number density is obtained by minimizing $\Omega[\rho]$ for appropriate choices of the functional $F[\rho]$ and of the substrate potential $V(\boldsymbol{r})$. Here, Rosenfeld's fundamental measure theory is employed for that contribution to $F[\rho]$ which is due to the repulsive part of the interaction among the fluid particles; this approach is known to accurately describe molecular details of the structure of simple liquids in confinement.[25–27] The attractive part of the fluid–fluid interaction is treated in a mean field fashion using forces of the van der Waals type cut off at distances larger than 2.5σ. The geometrical and chemical features of the wall can be tuned by changing $V(\boldsymbol{r})$, *e.g.*, to render walls with grooves (see Fig. 1 and the Appendix). The characteristic length and energy scales of the system are set by the fluid particle diameter σ and by the fluid–fluid Lennard-Jones interaction parameter ε. For further details concerning the implementation of the DFT see the Appendix and ref. 27 and 28.

The geometry of the system is illustrated schematically in Fig. 1(a). Before introducing surface structures, the substrate occupies the lower half-space and is associated with Young's contact angle θ_Y. For each particular system, θ_Y is computed *via* independent calculations of the solid–vapor (γ_{sv}), solid–liquid (γ_{sl}), and liquid–vapor (γ_{lv}) interfacial tensions following Young's law $\cos\theta_Y \equiv (\gamma_{sv} - \gamma_{sl})/\gamma_{lv}$. In a second step, a rectangular groove of height h and width w is excavated from the solid material. Calculations of the wetting and dewetting processes in such grooves are performed using a DFT code[28] applying periodic boundary conditions in the x and y directions. In these calculations the same mesh width of the computational grid has been used as in those carried out in order to determine θ_Y. The temperature is kept fixed at $T = 0.71T_c$, where T_c is the critical temperature of the bulk fluid.

3 Results and discussion

3.1 Pressure of the "groove"-liquid spinodal

In order to follow the metastable branch corresponding to the Cassie–Baxter (Wenzel) state at various pressures, we use initial conditions with the groove being filled with vapor (liquid). In a second step, we minimize the grand potential in eqn (1) in

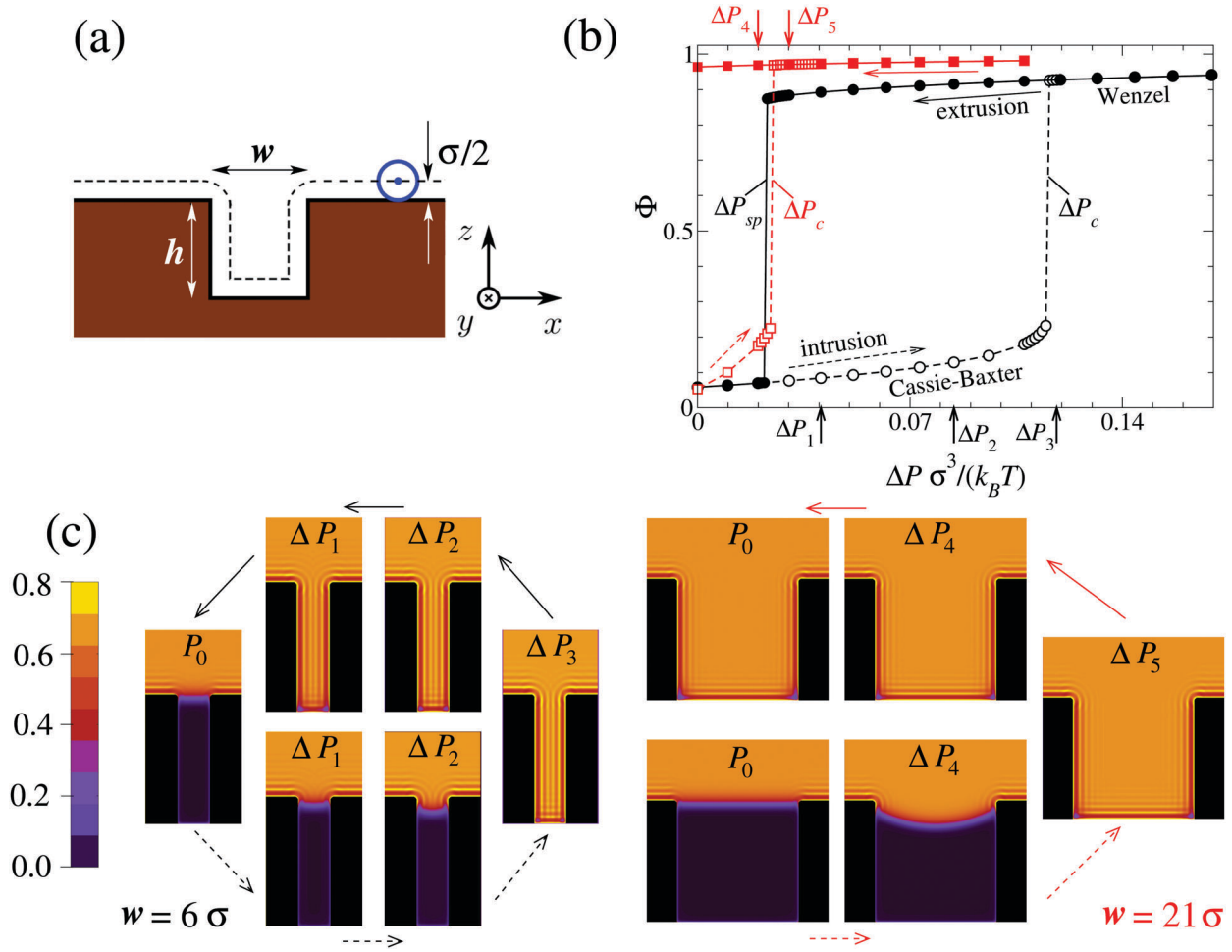

Fig. 1 Intrusion and extrusion of liquid in nano-grooves with fixed height $h = 20\sigma$ and for two widths $w = 6\sigma$ (black) and $w = 21\sigma$ (red); $\theta_Y = 121°$. (a) Definition of the system: the dashed line represents the distance of closest approach to the wall for the centers of the blue fluid particles of radius 0.5σ. (b) Filling fraction Φ of the groove as a function of the pressure difference $\Delta P \equiv P - P_0$, where P_0 is the pressure of liquid–vapor coexistence in the bulk at $T/T_c = 0.71$. The intrusion (dashed lines, open symbols) and extrusion (solid lines, full symbols) curves are obtained from (meta)stable DFT (see the main text and the Appendix). All symbols correspond to the bulk liquid phase, *i.e.*, $P - P_0 \geq 0$. (c) Number density distributions in units of σ^3 along the intrusion and extrusion branches.

order to obtain $\rho(\boldsymbol{r})$; the next point in the intrusion (extrusion) curve is obtained by initializing the system with the previous $\rho(\boldsymbol{r})$ and increasing (decreasing) the pressure as shown by the dashed (solid) arrows in Fig. 1. Black (red) arrows correspond to $w = 6\sigma$ ($w = 21\sigma$). In particular, Fig. 1(b) reports the filling fraction $\Phi \equiv N/(\rho_l V_g)$ of the groove as a function of the pressure in the reservoir, while Fig. 1(c) shows the color-coded distribution $\rho(\boldsymbol{r})\sigma^3$ which illustrates quantitatively the intrusion and extrusion processes. Here $N \equiv \int_{D_g} \rho(\boldsymbol{r}) \mathrm{d}^3 r$ is the number of fluid particles inside the domain D_g of the groove; ρ_l is the bulk liquid density at the corresponding pressure and $V_g = \int_{D_g} \mathrm{d}^3 r = w \times h \times \Delta y$, with Δy being the groove extension in the y direction.

Fig. 1(b) shows that at the critical pressure $P_c = \Delta P_c + P_0$ the intrusion branch jumps from the suspended Cassie–Baxter state (small Φ) to the completely filled Wenzel one (large Φ): P_c is the maximum pressure at which superhydrophobicity can survive, before it becomes mechanically unstable. It is well known that narrow grooves exhibit larger values of P_c (see the discussion below). What is more surprising in Fig. 1 is that for $w = 6\sigma$ the extrusion branch jumps from the Wenzel state to the Cassie–Baxter state: this is the sought liquid spinodal pressure $P_{sp} > 0$ in confinement (for $w = 21\sigma$ (red) ΔP_{sp} is negative). For $P \leq P_{sp}$, the Wenzel state is unstable and superhydrophobicity becomes perpetual.

In order to understand how P_{sp} depends on the characteristics of the surface, we performed DFT calculations similar to those leading to Fig. 1 for grooves with various widths and contact angles. The results reported in Fig. 2 show that by increasing the lyophobicity of the surface (*i.e.*, upon increasing Young's contact angle θ_Y) the Wenzel state can still be eliminated at $\Delta P_{sp} > 0$ even from increasingly wide grooves, up to $w = 21\sigma$ (see red squares in Fig. 2). In summary, confinement and lyophobicity cooperate towards increasing P_{sp} and can be engineered in order to obtain perpetual superhydrophobicity. By adopting a typical parameter value $\sigma = 0.34$ nm corresponding to the Lennard-Jones

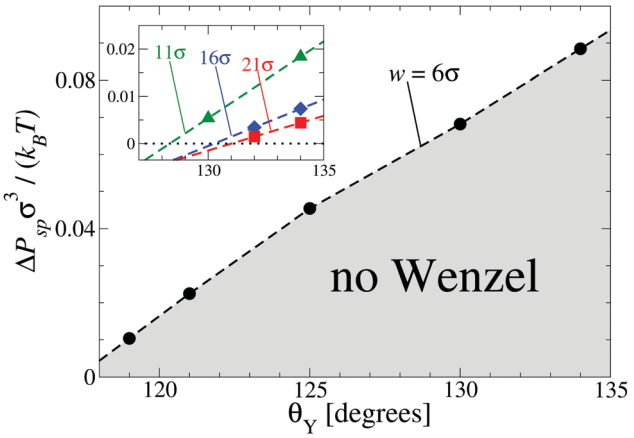

Fig. 2 Liquid spinodal pressure $\Delta P_{sp} \equiv P_{sp} - P_0$ as a function of Young's contact angle θ_Y for rectangular grooves with fixed height $h = 20\sigma$ and with widths $w = 6\sigma$ (black), $w = 11\sigma$ (green), $w = 16\sigma$ (blue), and $w = 21\sigma$ (red). For $\Delta P < \Delta P_{sp}(\theta_Y)$ the Wenzel state is eliminated.

potential for Argon[29] and setting $T = 300$ K, one can estimate that, for $\theta_Y = 134^\circ$, in the case $w = 6\sigma$ the Wenzel state remains eliminated up to $\Delta P = \Delta P_{sp}(\theta_Y) \simeq 9.3$ MPa and in the case $w = 21\sigma$ up to $\Delta P \simeq 0.5$ MPa.

3.2 Grooves *versus* infinite slits

We now elucidate the influence of the substrate morphology on the liquid spinodal. We first calculate, *via* the same microscopic DFT, the (meta)stable states of the considered fluid in a slit pore of width w and confined between two infinitely extended planar walls having the same Young contact angle as the substrate from which the grooves in Fig. 1 are excavated. The slit pore calculations are performed *via* a 1d numerical code. In this well known case the two states to be considered are the capillary vapor and the capillary liquid.[30] For $\theta_Y = 121^\circ$ the capillary liquid spinodal occurs at $\Delta P_{sp} > 0$ only for slit pores with $w < 3\sigma$ (solid red line in Fig. 3(a)). In the case of grooves, however, the groove-liquid spinodal occurs at $\Delta P_{sp} > 0$ already for $w \lesssim 6\sigma$ (blue square). This demonstrates that the destabilization of the confined liquid is facilitated by the groove geometry. For the systems shown in Fig. 1 the groove height is sufficiently large to ensure that the upper portion of the groove *de facto* does not shift the liquid spinodal. Therefore, the density oscillations induced at the two corners at the groove bottom and at the bottom wall seem to be the main reason for the shift of the spinodal towards higher pressures as compared to a slit with the same width. It is useful to remark that this effect differs from wedge drying, because (i) $\theta_Y < 135^\circ$ and (ii) the presence of a single corner is insufficient to obtain $\Delta P_{sp} \geq 0$ as demonstrated by the results for grooves with $w > 21\sigma$, for which $\Delta P_{sp} < 0$.

The shift of the spinodal is caused by the strong layering in the liquid induced by the confinement (Fig. 3(c)): the layers form "interference-like" patterns within the groove, which become "destructive" for the liquid at the bottom corners. This triggers a density depletion at the bottom corners, which is further enhanced by the increased lyophobicity of the walls near the corners due to the "missing" fluid–fluid interactions

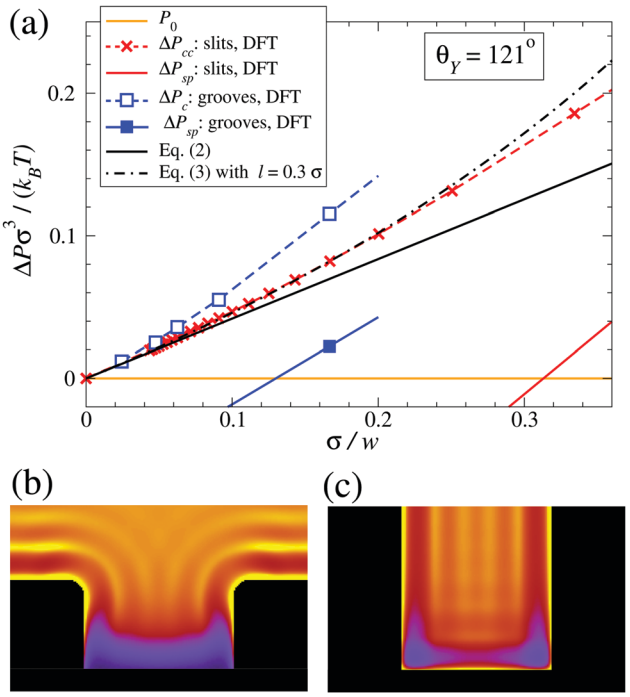

Fig. 3 Summary of the main findings for lyophobic ($\theta_Y = 121^\circ$) confined systems (rectangular grooves and slit pores). (a) Bulk liquid–vapor coexistence (orange) as well as capillary liquid and capillary vapor coexistence for slits at ΔP_{cc} (red crosses, interpolated by the dashed red line); Kelvin–Laplace law (eqn (2), solid black line); corrected Kelvin–Laplace law with $l = 0.3\sigma$ (eqn (3), dash-dotted black line). Concerning rectangular grooves, the interpolated open blue and solid blue squares represent ΔP_c and ΔP_{sp}, respectively; a second solid blue square occurs at $\Delta P_{sp} < 0$ and is not shown. Enlarged views of the liquid layering (b) near the top corners in the Cassie–Baxter state and (c) at the bottom corners in the Wenzel state for rectangular grooves with $w = 6\sigma$ at the same pressure $\Delta P \gtrsim \Delta P_{sp}$.

at the corners as compared to a planar wall. For narrow grooves these depletion zones at the bottom corners become connected (see Fig. 3(c)) favoring the growth of a bubble and thus the formation of the Cassie–Baxter state. This mechanism has some resemblance to dewetting *via* the growth of unstable surface waves (see, *e.g.*, Herminghaus *et al.*[31]). Evans and Stewart recently discussed how the local compressibility is enhanced at a lyophobic wall, thereby enhancing the density fluctuations;[32] the present results suggest that the enhancement is even stronger at corners.

Another important parameter to characterize superhydrophobicity is the critical pressure P_c for which the Cassie–Baxter state ceases to be mechanically stable (Fig. 1(b)). At the macroscopic level of description P_c is determined by balancing the hydrostatic pressure, as given by the Laplace law, and the z component of the capillary forces acting upon the contact line due to the liquid–vapor surface tension γ_{lv}. In the case of rectangular grooves this force balance renders the Kelvin–Laplace law:

$$\Delta P_c \equiv P_c - P_0 = -\frac{2\gamma_{lv}\cos\theta_Y}{w}. \qquad (2)$$

The very same equation applies to the capillary condensation pressure $\Delta P_{cc} \equiv P_{cc} - P_0$ at which the capillary-liquid and the

capillary-vapor coexist in (macroscopic) slit pores, see, *e.g.*, ref. 30.

It is known that the Kelvin–Laplace law can be improved on the mesoscale by accounting for the formation of wetting films at the walls of the slit pore.[33,34] This gives rise to the correction

$$\Delta P_{\mathrm{c,meso}} = -\frac{2\gamma_{\mathrm{lv}}\cos\theta_{\mathrm{Y}}}{w-3l}, \qquad (3)$$

where l is the thickness of the liquid wetting film; in the present case it is of atomic size.[34]

As shown in Fig. 3(a), the Kelvin–Laplace law, eqn (2), accurately predicts ΔP_{c} for grooves with $w \geq 15\sigma$. In the same range, eqn (2) also captures ΔP_{cc} (dashed red line). For grooves and slit pores with $w \leq 15\sigma$ both ΔP_{c} and ΔP_{cc}, as obtained by DFT, are larger than what is predicted by eqn (2). More specifically, ΔP_{cc} falls in between ΔP_{c} and the Kelvin–Laplace law. By using $l = 0.3\sigma$, which is within a plausible range, as a fit parameter in eqn (3), we obtain a good agreement between ΔP_{cc} and $\Delta P_{\mathrm{c,meso}}$ for $w > 4\sigma$ (black dash-dotted line). In contrast to the macroscopic predictions, we find that the critical pressure ΔP_{c} for intrusion is different from the capillary condensation pressure ΔP_{cc}. Actually ΔP_{c} is significantly higher than ΔP_{cc} for small groove widths w. Before we discuss the physics behind this observation we also have to exclude potential numerical errors which could influence this result. First, ΔP_{cc} is calculated by equating the free energies of a slit either filled with capillary liquid or with capillary vapor. Although within this treatment there is no explicit force balance at a liquid–vapor interface, the coexistence pressure, defined *via* the pressure in the reservoir, must be the same as one would obtain from a search for an indifferent liquid–vapor interface position in the slit. Numerics should not spoil this identity if otherwise the same conditions are chosen. A more serious source of error could be in the determination of ΔP_{c} because the iterative computation of the fluid number densities close to the critical intrusion pressure converges very slowly. In order to ensure that metastable configurations have indeed been found and that, in the vicinity of the critical pressure, the appropriate intrusion pressure has not been missed, we carried out computations starting from distinct initial positions of the liquid–vapor interface and we increased the number of calculated pressures (see Fig. 1(b)). The error in ΔP_{c} is estimated to be considerably smaller than the difference between ΔP_{c} and ΔP_{cc}.

With this we turn to the physical mechanism which can lead to the observed difference between ΔP_{c} and ΔP_{cc}. It has to be linked to the fact that a groove, in contrast to an infinite slit, has an open upper end and a capped bottom. Therefore, the wetting properties of a segment of a groove side wall depend on its depth in the groove, *i.e.*, on its distance, say, from the upper corner. In a coarse picture, the wetting properties of a wall are determined by a balance of the loss of fluid–fluid interactions *versus* the gain in fluid–solid interactions due to the presence of the wall. For the lyophobic walls, as discussed here, one expects that the wall segments close to the upper corner are less lyophobic than an infinitely extended wall because less of the fluid–fluid interaction is replaced by the weaker fluid–solid interaction. Deeper in the groove the side wall segments become more lyophobic and, for a very deep groove, the wetting properties approach those of an infinitely extended slit. The precise characteristics of these effective properties of the wall depend on the details of the system. These generic considerations explain our observation of a partial intrusion. Liquid intrusion starting from the open upper end of the groove may progress to some depth below the open upper end where the side walls are less lyophobic, but it is stopped deeper in the groove as a result of the side walls becoming increasingly lyophobic (Fig. 3(b)). Whether the critical intrusion pressure ΔP_{c} is larger than ΔP_{cc} or not might depend on details of the shapes of the fluid–solid as well as of the fluid–fluid interaction. In our model the attractive part of both interactions is of the van der Waals type with, however, the fluid–fluid interaction cut off at 2.5σ. Therefore, at some distance below the upper corner of the groove the side wall of the groove becomes more lyophobic than an infinitely extended wall of the same material, because the missing fluid–solid interactions are still appreciable whereas the fluid–fluid interactions are cut off. This would lead to an enhancement of ΔP_{c} over ΔP_{cc} with the latter being based on the properties of infinitely extended walls. Of course intrusion into grooves is influenced additionally by specific confinement effects which become very pronounced for very small groove widths. For instance, the liquid–vapor interface at the open upper end of the groove has a structure (see Fig. 3(b)) which deviates significantly not only from that of a free liquid–vapor interface, but also from that between capillary liquid and capillary vapor deep inside the groove, which is a transient unstable configuration.

In order to summarize our remarks, deviations between ΔP_{cc} and the Kelvin–Laplace law arise because for very narrow slits, due to various confinement effects, the force balance at a liquid–vapor interface in an infinitely extended slit cannot be reliably characterized in terms of size independent surface and interfacial tensions. Deviations between ΔP_{c} and ΔP_{cc} can occur because even quite deep into a groove the force balance at a liquid–vapor interface might still deviate from that in an infinitely extended slit; ΔP_{c} is determined by the highest pressure required to push the liquid through the open upper end and further into the groove. In the present case, the two upper corners effectively enhance the lyophobicity of the groove, resulting in $\Delta P_{\mathrm{c}} > \Delta P_{\mathrm{cc}}$. In the general case, whether ΔP_{c} is effectively enhanced over ΔP_{cc} and to which extent will presumably depend on the detailed shapes of the fluid–solid and fluid–fluid interactions.

3.3 Hierarchical structures

In many applications, nano-structures such as those proposed here for realizing perpetual superhydrophobicity are too small to achieve effects of technological relevance. Important examples are submerged surfaces for drag reduction,[3] in which slippage increases with the characteristic dimension of the texture.[35] In such cases, and if it is advantageous to maximize the air volume of the Cassie–Baxter state, larger textures, say above one micrometer, should be used. Larger structures are also more resistant

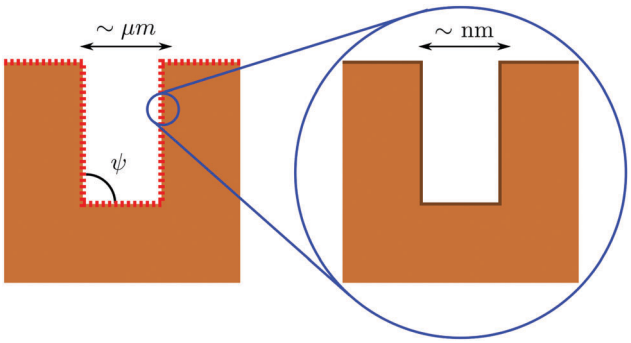

Fig. 4 Illustration of the concept of hierarchical surface structures for perpetual superhydrophobicity: two tiers are present, one on the nanometer scale, which realizes a perpetual nano-Cassie–Baxter state, and the other on the micrometer (or larger) scale, which inherits the "unbreakability" of the smaller scale.

to mechanical wear.[36] However, the composite interface associated with that scale is very fragile such that the ensuing superhydrophobic state easily breaks down into the Wenzel state, due to the very low corresponding values of ΔP_c (see eqn (2)). In order to increase the stability of a composite interface, surfaces with multiscale hierarchical structures, as illustrated schematically in Fig. 4, have been suggested, *e.g.*, in ref. 16 and 37.

Here we propose the concept of perpetual superhydrophobicity, *i.e.*, complete thermodynamic elimination of the Wenzel state, also for micron-sized geometrical textures. The basic idea is to utilize hierarchical surface structures, which exploit the perpetual superhydrophobicity of the nano-scale textures described above, in combination with the so-called wedge drying phenomenon[38–40] at larger scales. Micron-sized wedges immersed in a liquid at bulk liquid–vapor coexistence, *i.e.*, at $\Delta P = 0$, exhibit spontaneous drying when the condition

$$\theta_Y = \frac{\pi + \psi}{2} \tag{4}$$

is met,[41] where ψ is the opening angle of the lower corners of the larger texture (Fig. 4). Thus, for rectangular wedges the (macroscopic) drying transition is expected to occur for $\theta_Y > 135^\circ$ at $\Delta P = 0$. It is worth noting that such large contact angles can be rarely achieved for flat surfaces. However, as we shall argue below, this can be easily realized if the walls forming the micro-structure themselves carry a secondary nano-structure. The latter coating must fullfill the following two requirements. First, the nano-structure must realize perpetual superhydrophobicity over the whole desired pressure range (Fig. 2). Second, the Cassie–Baxter state associated with the nano-structure must exhibit sufficiently low liquid–solid contact in order to weaken the attraction between the liquid and the surface. This attraction can be quantified by means of the effective contact angle θ_{eff} defined in terms of the excess surface free energy per projected area:

$$\cos\theta_{eff} = \frac{\Omega_{0,vs} - \Omega_{0,ls}}{A\gamma_{lv}}, \tag{5}$$

where $\Omega_{0,vs}$ is the free energy at $\Delta P = 0$ of the solid exposed to the vapor, $\Omega_{0,ls}$ is the free energy at $\Delta P = 0$ for the nano-sized Cassie–Baxter configuration, and A is the projected area of the substrate surface. By introducing this definition, the nano-corrugated surface exposed to the fluid is effectively treated as a planar but chemically heterogeneous surface with area A. This effective planar surface may be thought of as being composed of the solid patches providing solid–fluid interfaces, and patches above the vapor pockets, trapped inside the structure, providing vapor–fluid (vapor–liquid and "vapor–vapor") interfaces. The area fraction forming a solid–fluid interface is denoted as ϕ_s. Note that the distinct contributions to Ω_0 from the two types of vapor pockets trapped inside the nano-grooves (see above) are essentially identical to each other and they approximately cancel each other in the difference in eqn (5). The angle θ_{eff} also gives the contact angle at which a macroscopic liquid–vapor interface intersects the nano-structured surface, provided their intersection line samples the solid patches and the vapor pockets according to their respective area fractions ϕ_s and $1 - \phi_s$, respectively. We further argue that for $\theta_{eff} > 135^\circ$ wedge drying occurs also for the considered nano-structured surfaces, similar to the case of a planar homogeneous wall characterized by $\theta_Y > 135^\circ$.

Within our model we computed θ_{eff} *via* DFT for a nano-groove with $w = 6\sigma$, $\theta_Y = 121^\circ$, and a solid fraction $\phi_s = 1/2$ yielding $\theta_{eff} = 141^\circ$. This result is in fair agreement with the macroscopic estimate $\theta_{CB} \simeq 139^\circ$ obtained by using the well-known macroscopic Cassie–Baxter equation[42] $\cos\theta_{CB} = \phi_s(\cos\theta_Y + 1) - 1$ for describing the contact angle θ_{CB} of sessile droplets in the so-called "fakir regime".[43] In deriving this Cassie–Baxter equation, in the first step, effective solid–fluid interfacial tensions are calculated as area weighted averages of the solid–fluid and vapor–fluid interfacial tensions, which characterize the patches forming the actual surface. In the second step, these effective interfacial tensions are used in Young's law leading to the above expression for $\cos\theta_{CB}$. In order to support the proposed wedge-drying mechanism for restoring the Cassie–Baxter state on the micro-scale, the nano-sized surface structure must be in the Cassie–Baxter state which is guaranteed if it is perpetual. Otherwise, once the liquid has intruded the nano-texture, a nucleus of vapor forming at the edge of a wedge cannot grow, even if it is favored thermodynamically for $\theta_Y > 135^\circ$, as the result of strong pinning of the liquid–vapor interface near the intruded liquid pockets. Therefore, in this case the proposed wedge-drying mechanism becomes ineffective. In contrast to that, in the nano-sized Cassie–Baxter state this pinning is much weaker and we expect this mechanism to be effective.

4 Conclusions

Microscopic density functional theory has shown that the fragility of the superhydrophobic state can be entirely healed by a combination of nano-scale surface texturing (*ca.* 2 nm) and lyophobic coating ($\theta_Y = 121^\circ$). Nanoconfinement shifts the

liquid spinodal to very large pressures, up to 2.4 MPa, completely eliminating the Wenzel state over this very broad range of pressures. Thus the proposed passive strategy is expected to be robust against thermal fluctuations and abrupt changes in the liquid pressure. In addition, the critical pressure for the transition of the Cassie–Baxter state to the Wenzel state is also increased by nano-confinement, more than what can be expected based on the Kelvin–Laplace law (eqn (2)). Both effects are highly beneficial for the applications of superhydrophobicity and call for thorough wetting experiments on nano-structured surfaces. Based upon these properties of the nano-textured surfaces, hierarchical structures could be designed which would also support perpetual superhydrophobicity at the micro-scale. Here, the key requirements for the nano-textures are: (i) the occurrence of the spinodal of the nano-confined liquid at $\Delta P_{sp} > 0$; and (ii) sufficiently large values of the effective Cassie–Baxter contact angle.

Appendix: density functional theory

In this study we use the fundamental measure theory (FMT) due to Rosenfeld,[25,26] which has been implemented into an in-house numerical code as described already elsewhere.[28] Further details on this type of classical density functional theory are found in the review by Roth.[27]

Here we describe the computational domains used for obtaining the intrusion and extrusion curves presented above. The densities have been discretized on a grid and in most calculations a mesh size of 0.05σ has been used. For comparison some computations have been repeated with a smaller mesh size of 0.025σ. From a semi-infinite wall occupying the lower half space, a parallelepipedic groove is excavated (Fig. 5). The height of the groove is fixed to the value $h = 20\sigma$ while various widths are considered: $w = 6\sigma$, $w = 11\sigma$, $w = 16\sigma$, $w = 21\sigma$, and $w = 41\sigma$. Since for technical reasons we have used a 3D DFT, despite the translational invariance of the system in the y direction, our computational box has a finite extent in this direction for which we have chosen periodic boundary conditions. In order to speed up the calculations, actually only one half of the domain is considered, applying symmetric boundary conditions to the left side of the domain (see Fig. 5). To the right side also reflecting boundary conditions are applied which are equivalent to having a mirror symmetry plane along the y–z plane, *i.e.*, we effectively treat a periodic array of grooves aligned along the y axis. The box dimensions in the x direction have been chosen such that the ridge separating the grooves has a width of 20σ. A constant number density is imposed at the top boundary of the computational box, which is equivalent to prescribing the pressure in the system far away from the wall. At the bottom boundary there is the wall.

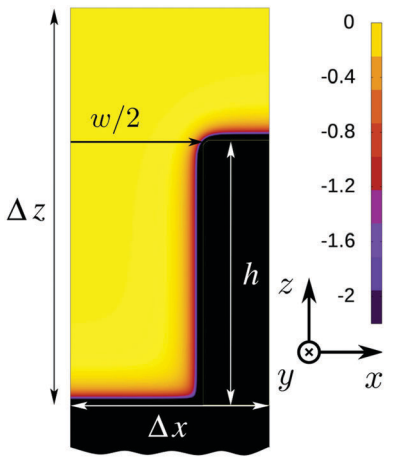

Fig. 5 Color-coded wall potential $V(\boldsymbol{r})$ in units of ε for a groove of width $w = 21\sigma$ and height $h = 20\sigma$. The actual computational domain used in this study has the size $\Delta x \times \Delta y \times \Delta z = 20.5\sigma \times 5\sigma \times 35.5\sigma$.

The external substrate potential $V(\boldsymbol{r})$ is the sum of a repulsive contribution $V_{rep}(\boldsymbol{r})$ and an attractive one $V_{att}(\boldsymbol{r})$: $V(\boldsymbol{r}) = V_{rep}(\boldsymbol{r}) + V_{att}(\boldsymbol{r})$. We account for $V_{rep}(\boldsymbol{r})$ in terms of a hard-sphere repulsion, chosen such that the distance of closest approach is $\sigma/2$, *i.e.*, the radius of the fluid particles. $V_{rep}(\boldsymbol{r})$ is set to infinity inside the zone of closest approach. $V_{att}(\boldsymbol{r})$ is taken as the linear superposition of the attractive part Φ_w of a Lennard-Jones potential between the fluid particles and the particles forming the wall with a number density ρ_w:

$$V_{att}(\boldsymbol{r}) = \int_{D_w} d^3r' \rho_w \Phi_w(\boldsymbol{r} - \boldsymbol{r}'). \quad (6)$$

Here the fluid–wall pair potential $\Phi_w(\boldsymbol{r} - \boldsymbol{r}')$, which depends on the distance between the positions $\boldsymbol{r}$ and $\boldsymbol{r}'$ of the fluid and wall particles, respectively, is integrated over the domain D_w occupied by the wall; $\Phi_w(\boldsymbol{r} - \boldsymbol{r}') = -4\varepsilon_w(\sigma_w/|\boldsymbol{r} - \boldsymbol{r}'|)^6$ (σ_w may be considered to characterize the diameter of a wall particle). The strength of the wall potential is determined by the parameter combination $u_w \equiv (2\pi/3)n_w\varepsilon_w$ where $n_w = \rho_w\sigma_w^3$ is the number of wall particles in the volume σ_w^3. Instead of using this wall strength we have chosen to characterize the fluid–wall interaction by the contact angles computed using Young's law. (In addition, Young's contact angle depends on the ratio between the fluid–fluid Lennard-Jones interaction parameter and k_BT which is kept fixed in all computations and given by our choice $T = 0.71T_c$ of the temperature.) Actually, for the mesh width 0.05σ used in most of our calculations, the computed contact angles may be still off their fully converged values by several degrees. However, our control computations using finer meshes (mesh width 0.025σ) show that essentially identical spinodal or critical pressures are found, if we compare computations with the wall strengths tuned such that the contact angles for the finer and the coarser grid are the same. This implies that the contact angle is a measure of the fluid–wall interaction which is quite robust against discretization errors, provided all computations are carried out on the same grid.

The pressure is calculated from the following bulk equation of state (which corresponds to the density functional which is used here):

$$P(\eta, T) = \frac{6k_BT\eta}{\pi\sigma^3}\left(\frac{1 + \eta + \eta^2}{(1 - \eta)^3} + \frac{1}{2}B_{lr}\eta\right) \quad (7)$$

where $\eta = \pi\sigma^3\rho/6$ is the packing fraction, and B_{lr} is related to the integrated strength of the long-ranged attractive part of the

fluid–fluid interaction potential $u_{lr}(r)$ as $B_{lr} = 6\int_{\mathbb{R}^3} u_{lr}(r)\mathrm{d}^3 r/(\pi\sigma^3)$. The chemical potential μ of the reservoir can be expressed as a function of η and T:

$$\mu(\eta, T) = k_B T\left(-\ln(1-\eta) + \frac{\eta}{1-\eta}\left(7 + \frac{15\eta}{2(1-\eta)} + \frac{3\eta^2}{(1-\eta)^2}\right) + B_{lr}\eta\right). \quad (8)$$

The density (or, equivalently, the pressure) is always chosen to lie either on the liquid side or at liquid–vapor coexistence of the bulk phase diagram. The computational domain has a total extent of $\Delta x \times \Delta y \times \Delta z = (w/2 + 10\sigma) \times 5\sigma \times 35.5\sigma$. This domain is discretized with 20 points per σ for a total of *ca.* 40 millions of points for the domain in Fig. 5.

References

1 W. Barthlott and C. Neinhuis, *Planta*, 1997, **202**, 1–8.
2 A. Tuteja, W. Choi, J. M. Mabry, G. H. McKinley and R. E. Cohen, *Proc. Natl. Acad. Sci. U. S. A.*, 2008, **105**, 18200–18205.
3 J. P. Rothstein, *Annu. Rev. Fluid Mech.*, 2010, **42**, 89–109.
4 T. Liu and C. Kim, *Science*, 2014, **346**, 1096–1100.
5 A. Lafuma and D. Quéré, *Nat. Mater.*, 2003, **2**, 457–460.
6 A. Giacomello, M. Chinappi, S. Meloni and C. M. Casciola, *Phys. Rev. Lett.*, 2012, **109**, 226102.
7 T. Koishi, K. Yasuoka, S. Fujikawa, T. Ebisuzaki and X. Zeng, *Proc. Natl. Acad. Sci. U. S. A.*, 2009, **106**, 8435–8440.
8 A. Giacomello, S. Meloni, M. Chinappi and C. M. Casciola, *Langmuir*, 2012, **28**, 10764–10772.
9 A. Checco, B. Ocko, A. Rahman, C. T. Black, M. Tasinkevych, A. Giacomello and S. Dietrich, *Phys. Rev. Lett.*, 2014, **112**, 216101.
10 T. N. Krupenkin, J. A. Taylor, E. N. Wang, P. Kolodner, M. Hodes and T. R. Salamon, *Langmuir*, 2007, **23**, 9128–9133.
11 R. J. Vrancken, H. Kusumaatmaja, K. Hermans, A. M. Prenen, O. Pierre-Louis, C. W. Bastiaansen and D. J. Broer, *Langmuir*, 2009, **26**, 3335–3341.
12 G. Manukyan, J. Oh, D. Van Den Ende, R. Lammertink and F. Mugele, *Phys. Rev. Lett.*, 2011, **106**, 014501.
13 Z. Cheng, H. Lai, N. Zhang, K. Sun and L. Jiang, *J. Phys. Chem. C*, 2012, **116**, 18796–18802.
14 G. Liu, L. Fu, A. V. Rode and V. S. Craig, *Langmuir*, 2011, **27**, 2595–2600.
15 M. Amabili, A. Giacomello, S. Meloni and C. M. Casciola, *Adv. Mater. Interfaces*, 2015, **2**, 1500248.
16 T. Verho, J. T. Korhonen, L. Sainiemi, V. Jokinen, C. Bower, K. Franze, S. Franssila, P. Andrew, O. Ikkala and R. H. Ras, *Proc. Natl. Acad. Sci. U. S. A.*, 2012, **109**, 10210–10213.
17 Q. Zheng, D. J. Durben, G. H. Wolf and C. A. Angell, *Science*, 1991, **254**, 829–832.
18 M. El Mekki Azouzi, C. Ramboz, J.-F. Lenain and F. Caupin, *Nat. Phys.*, 2013, **9**, 38–41.
19 D. Bérard, P. Attard and G. Patey, *J. Chem. Phys.*, 1993, **98**, 7236–7244.
20 K. Lum, D. Chandler and J. D. Weeks, *J. Phys. Chem. B*, 1999, **103**, 4570–4577.
21 D. Bratko, R. Curtis, H. Blanch and J. Prausnitz, *J. Chem. Phys.*, 2001, **115**, 3873–3877.
22 T. M. Truskett, P. G. Debenedetti and S. Torquato, *J. Chem. Phys.*, 2001, **114**, 2401–2418.
23 A. Luzar, *J. Phys. Chem. B*, 2004, **108**, 19859–19866.
24 S. Prakash, E. Xi and A. Patel, *Proc. Natl. Acad. Sci. U. S. A.*, 2016, **113**, 5508–5513.
25 Y. Rosenfeld, *Phys. Rev. Lett.*, 1989, **63**, 980–983.
26 Y. Rosenfeld, M. Schmidt, H. Löwen and P. Tarazona, *Phys. Rev. E: Stat. Phys., Plasmas, Fluids, Relat. Interdiscip. Top.*, 1997, **55**, 4245–4263.
27 R. Roth, *J. Phys.: Condens. Matter*, 2010, **22**, 063102.
28 S. L. Singh, L. Schimmele and S. Dietrich, *Phys. Rev. E: Stat., Nonlinear, Soft Matter Phys.*, 2015, **91**, 032405.
29 A. Rahman, *Phys. Rev.*, 1964, **136**, A405–A411.
30 R. Evans, U. Marini Bettolo Marconi and P. Tarazona, *J. Chem. Phys.*, 1986, **84**, 2376–2399.
31 S. Herminghaus, K. Jacobs, K. Mecke, J. Bischof, A. Fery, M. Ibn-Elhaj and S. Schlagowski, *Science*, 1998, **282**, 916–919.
32 R. Evans and M. C. Stewart, *J. Phys.: Condens. Matter*, 2015, **27**, 194111.
33 B. V. Derjaguin, *Acta Physicochim. URSS*, 1940, **12**, 181.
34 R. Evans and U. Marini Bettolo Marconi, *Chem. Phys. Lett.*, 1985, **114**, 415–422.
35 C. Ybert, C. Barentin, C. Cottin-Bizonne, P. Joseph and L. Bocquet, *Phys. Fluids*, 2007, **19**, 123601.
36 X. Tian, T. Verho and R. H. A. Ras, *Science*, 2016, **352**, 142–143.
37 B. Bhushan, Y. C. Jung and K. Koch, *Philos. Trans. R. Soc., A*, 2009, **367**, 1631–1672.
38 R. Roth and A. O. Parry, *Mol. Phys.*, 2011, **109**, 1159–1167.
39 R. Roth and A. O. Parry, *J. Phys. Soc. Jpn.*, 2012, **81**, SA009.
40 A. Malijevský and A. O. Parry, *Phys. Rev. E: Stat., Nonlinear, Soft Matter Phys.*, 2015, **91**, 052401.
41 K. Rejmer, S. Dietrich and M. Napiórkowski, *Phys. Rev. E: Stat. Phys., Plasmas, Fluids, Relat. Interdiscip. Top.*, 1999, **60**, 4027–4042.
42 A. B. D. Cassie and S. Baxter, *Trans. Faraday Soc.*, 1944, **40**, 546–551.
43 Z. Yoshimitsu, A. Nakajima, T. Watanabe and K. Hashimoto, *Langmuir*, 2002, **18**, 5818–5822.

